On the applicability of cavitation erosion risk models with a URANS Solver

Melissaris, Themis; Bulten, Norbert; van Terwisga, Thomas

DOI
10.1115/1.4043169

Publication date
2019

Document Version
Final published version

Published in
Journal of Fluids Engineering, Transactions of the ASME

Themistoklis Melissaris[1]
Department of Propulsion Performance,
Wartsila Netherlands BV,
Drunen 5151 DM, The Netherlands;
Department of Maritime and Transport Technology,
Delft University of Technology,
Delft 6700 AA, The Netherlands
e-mail: themis.melissaris@wartsila.com

Norbert Bulten
Wartsila Netherlands BV,
Drunen 5151 DM, The Netherlands
e-mail: norbert.bulten@wartsila.com

Tom J. C. van Terwisga
Department of Maritime and Transport Technology,
Delft University of Technology,
Delft 6700 AA, The Netherlands;
Resistance & Propulsion,
Maritime Research Institute Netherlands (MARIN),
Wageningen 6700 AA, The Netherlands
e-mail: t.v.terwisga@marin.nl

On the Applicability of Cavitation Erosion Risk Models With a URANS Solver

In the maritime industry, cavitation erosion prediction becomes more and more critical, as the requirements for more efficient propellers increase. Model testing is yet the most typical way a propeller designer can, nowadays, get an estimation of the erosion risk on the propeller blades. However, cavitation erosion prediction using computational fluid dynamics (CFD) can possibly provide more information than a model test. In the present work, we review erosion risk models that can be used in conjunction with a multiphase unsteady Reynolds-averaged Navier–Stokes (URANS) solver. Three different approaches have been evaluated, and we conclude that the energy balance approach, where it is assumed that the potential energy contained in a vapor structure is proportional to the volume of the structure, and the pressure difference between the surrounding pressure and the pressure within the structure, provides the best framework for erosion risk assessment. Based on this framework, the model used in this study is tested on the Delft Twist 11 hydrofoil, using a URANS method, and is validated against experimental observations. The predicted impact distribution agrees well with the damage pattern obtained from paint test. The model shows great potential for future use. Nevertheless, it should further be validated against full scale data, followed by an extended investigation on the effect of the driving pressure that leads to the collapse. [DOI: 10.1115/1.4043169]

1 Introduction

Cavitation is the creation and intense collapse of vapor pockets in a liquid when exposed to low pressures. These vapor structures occur at locations where the local pressure drops to such low values that the liquid evaporates. The collapse of the bubbly clouds in regions of pressure recovery can be very violent, leading to vigorous and rapid pressure wave emissions. In case of a collapse very close to the surface wall, a microjet is formed. The microjet pierces the side of the bubble which is closest to the wall, resulting in a high "water hammer" pressure, felt as a pressure wave on the surface, followed by a stagnation pressure of lower magnitude, but longer duration [1]. If the impulsive pressure, which stems from either the pressure wave, originated from cloud collapse or the water hammer, or the impact of the microjet at the stagnation point, exceeds a certain threshold, then local damage is induced. That threshold depends strongly on the mechanical properties of the surface material.

In the maritime industry, propeller cavitation is basically unavoidable, and therefore accepted. Cavitation could be avoided, but this comes at the cost of efficiency or extra capital investments. Thus, it becomes essential to know when cavitation is not harmful in operation. Cavitation can be the origin of several negative effects, such as noise, vibrations, structural damage, power, and material loss. The later, cavitation erosion might be responsible for severe damage on the propeller blades, considerably decreasing the propeller efficiency. Thus, the prediction of cavitation dynamics in the vicinity of a propeller becomes extremely important, in order to assess cavitation erosion risk on the propeller surface.

Although the first attempt to analyze a cavitation problem and to quantify the erosive potential of a single bubble was made by Rayleigh [2] in 1917, any further progress in actually quantifying the erosion process has been slow. He investigated bubble dynamics and solved the problem of the collapse of an empty cavity in a large mass of liquid, leading the way toward an extensive investigation on cavitation and bubble dynamics [3,4]. Most of the findings on cavitation inception, formation of bubbles, formation of complex cavitation patterns are reported and summarized by Plesset and Prosperetti [5] and Brennen [6]. They already knew that the high-pressure peaks occurring during the implosion of a bubble were partly responsible for the damage of propeller blades. However, the bending of trailing edges could not be caused by single collapse, but from collective collapses and interaction of many neighboring bubbles [7]. Momentum considerations were used for analysis of the collapse of a cluster, until Mørch [8] included the influence of the emitted pressure wave of each cavity to the cluster collapse, in the energy balance equation. Isselin et al. [9], and Philipp and Lauterborn [10], tried to elucidate the mechanism of cavitation erosion by investigating collective effects from consecutive bubble collapses. They showed that the destructive effect of cavitation is mainly caused by the collapse of bubbles in close vicinity of the solid boundary. However, they only observed the effects of single bubbles omitting any interaction between bubbles or collective collapses of bubbly clouds. Therefore, a complete description of the cavitation dynamics and the erosion process still remains obscure.

Recent research, within the EU CaFE project,[2] has led to a better understanding of the various types of collapsing cavities that lead to material damage. However, there is still a lack of physical knowledge and of a detailed phenomenological description of the process leading to cavitation erosion. The notion that the aggressiveness of cavitation could be assessed through a consideration of energy conversion was already acknowledged by Hammitt [11] and a potential energy approach was first proposed by Vogel and Lauterborn [12]. Erosion will occur due to the concentration of mechanical energy on very small areas of the solid surface. This energy concentration results in high stress levels which can exceed the resistance of the material. However, which is the

[1]Corresponding author.

Contributed by the Fluids Engineering Division of ASME for publication in the Journal of Fluids Engineering. Manuscript received November 27, 2018; final manuscript received March 12, 2019; published online April 25, 2019. Assoc. Editor: Matevz Dular.

[2]http://cafe-project.eu

mechanism that contributes more to surface erosion, still remains unclear.

Plesset and Chapman [1] showed that the liquid jet can develop velocities high enough to explain cavitation damage. This approach was adopted by Dular et al. [13], proposing a cavitation erosion model based on experimental studies. He recently found that when the implosion is in the close vicinity of the wall, the most pronounced mechanism is the impact of the microjet. As we move further away from the wall, the impact of the microjet diminishes and the collapses of microscopic bubbles during the rebound become more aggressive [14]. On the other hand, Fortes-Patella and Reboud [15] investigated various material samples submitted to different cavitation conditions, and they concluded that the pressure wave emission that could be generated by spherical bubble and vortex collapses as well as by microjet formation seemed to be the mechanism responsible for the damage. Furthermore, they developed an original approach to estimate the cavitation aggressiveness, based on energy balance between vapor bubble collapse, emitted pressure wave, and neighboring solid wall response [16].

Franc and Michel [17] claimed that both hydrodynamic mechanisms, the shock wave and the microjet, give rise to high pressure pulses, with the same order of magnitude as the yield strength of usual metals. However, in case of a collective collapse, which is typically characterized by cascades of implosions [10,18], the emitted pressure waves of a particular bubble tend to enhance the collapse velocities of the neighboring bubbles, thus increasing the amplitude of their own pressure waves. Especially when these collapses are originated from vortical structures, the erosive potential can be enhanced, due to the formation of a foamy cloud triggering cascade mechanisms and the relatively long duration of the impact applied to the wall [17].

Bark et al. [19] also used an energy consideration to explain the risk of cavitation erosion. "The concentration or focusing of the collapse energy to a small domain of the solid surface is an obvious requirement for generation of cavitation erosion. A cavity can be associated with a potential energy," as has been already acknowledged [11,12]. When the cavity collapses, the potential energy, contained initially in the bubble, will first be transformed into kinetic energy of the surrounding flow. When the minimum cavity radius is reached, the energy is transformed into potential energy and acoustic wave energy, which is felt as a pressure pulse in the surrounding liquid with the maximum value at the cavity interface. Thus, there is a focusing effect for the kinetic as well as the potential energy. The potential energy is then again transformed into kinetic energy during the rebound of the cavity [20].

To return to the main question, it should be noted that individual pits, early visible during the development of cavitation erosion, are typically of fairly small scale, from a few μm up to mm size. Larger scale damage, like deeper pits or extensive erosion, is certainly generated by collective large scale collapsing cavities and cavitating vortices. "Vortex cavitation can be very erosive even though it is surrounded by a durable pressure lowering rotation. This rotation is however also the explanation for the high erosiveness. The rotation creates the high symmetry needed for a perfect focusing collapse toward a point" [19].

Considering all the aforementioned factors, Terwisga et al. [21] claimed that the concentrated vorticity (from vortical structures originated from sheet cavitation), forms a mechanism to break up a monolithic cavity and to concentrate all the resulting microbubbles in space. The radiated shock-waves caused by an implosion of one microbubble, where there is a focusing of energy, is then hypothesized to be sufficient to initiate a synchronized implosion of the cloud of microbubbles in the immediate vicinity. Thus, it is concluded that the most aggressive acoustic emission is originated from a collective microbubble collapse, while cavitating vortices may increase the aggressiveness due to effective focusing of the acoustic power in space and time.

The first objective of this work is to review physical models for predicting cavitation erosion, following suggestions from the literature. Similar endeavors have been made in the past [21,22], however, new numerical approaches have been proposed, and existing models have been further developed and tested within the last years. The complexity of the phenomenon, and the need to provide a reliable method to quantitatively predict (the risk of) cavitation erosion, renders the evaluation of such models a relevant task.

From an industrial point of view, where there is always a compromise between time and quality, the development of a quick and reliable method to assess cavitation erosion risk is required. Thus, the second objective of this paper is to evaluate the existing erosion models, and assess their applicability on an industrial/commercial pressure based unsteady Reynolds-averaged Navier–Stokes (URANS) solver. To this end, we have conducted a detailed verification and validation study on the Delft Twist 11 hydrofoil in wetted and cavitating flow condition. We conclude that the energy balance approach proposed by Fortes-Patella et al. [23] is the most favorable method to estimate cavitation erosion risk for marine applications. The implemented erosion model, based on the previous work of Leclercq et al. [24] and Schenke and van Terwisga [25], is modified in such a way to reduce the computational cost. The numerical predictions are compared with experimental observations of material damage [26], showing a good correlation.

2 Review of Cavitation Erosion Risk Models

Cavitation is being observed experimentally for more than half a century; however, the need of including cavitating flow computations, already in the design phase, renders numerical simulations for cavitation prediction more imperative. Especially, the prediction of cavitation erosion, particularly on marine propellers, is quite a challenging task, and even observation in a cavitation tunnel does not give the required confidence, due to the difficulty either to observe such a process or to estimate scalabillity effects of such flows. Thus, the direct prediction of the erosion risk in full scale applications, using computational fluid dynamics (CFD), becomes very important.

Several attempts have been made in the past decades to predict cavitation erosion without using a model test. Kato et al. [27] proposed a scenario for quantitative prediction of the impact force distribution on the solid surface caused by cavitation. It uses several simplified empirical relations, which need further experimental and theoretical verification, rendering such a method questionable for propellers and rudders. Bark et al. [19] provided guidelines to assess erosiveness from visual observations. This model could easily be applied on rather large-scale cavities, at a scale which can be predicted be contemporary CFD methods; however, it is mainly based on the observation of rebound cavities and the estimation of their violence, thus not applicable for incompressible[3] solvers, where the simulation of a rebound cavity is impossible. Terwisga et al. [21] encourage to combine this model with experimental observations and paint tests.

During the last decade, more detailed attempts have been made to describe the physical mechanisms for assessing the risk of cavitation erosion. Three erosion models have been proposed and are discussed in Secs. 2.1, 2.2, and 2.3: the energy balance approach by Fortes-Patella et al. [23], the erosion model by Dular and Coutier-Delgosha [28], and the collapse detector by Mihatsch et al. [29].

2.1 Erosion Model 1—Energy Balance Approach. This model by Fortes-Patella et al. [23] describes the physical mechanism of cavitation erosion based on the energy transfer through the shock wave emitted by the collapse of vapor structures (Fig. 1). The model consists of the four following stages:

(1) The shedding vapor structures of the cavitating flow start to collapse;

[3]We should specify that with incompressible solvers we mean that they treat the pure phases as incompressible, because compressibility is considered when phase transition occurs.

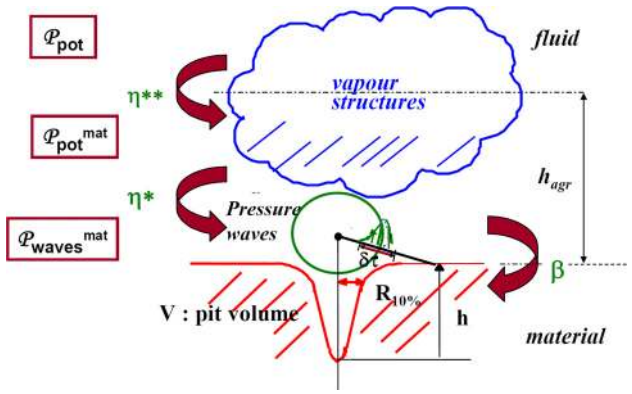

Fig. 1 Energy balance approach showing the transition of the energy contained in the initial vapor cavity to the material surface [30]

(2) The potential power, included in the vapor clouds, is converted into acoustic power through emitted pressure waves generated by the collapse. The pressure waves propagate toward the surface. It is suggested that those pressure waves are the main source contributing to the cavitation erosion;
(3) The emitted pressure waves interact with the solid surface
(4) The surface is exposed to material damage with a volume damage rate $\dot{V}_d$

The initial potential energy inside a vapor structure is defined as

$$E_{pot} = \Delta p \cdot V_\nu \tag{1}$$

where $\Delta p = (p_\infty - p_\nu)$, p_∞ is the surrounding pressure, p_ν is the vapor pressure, and V_ν is the vapor volume. Then, the instantaneous potential power can be defined as the Lagrangian time derivative of the potential energy

$$P_{pot} = -\Delta p(DV_\nu/Dt) \tag{2}$$

where the pressure derivative has been ignored [30], as it is assumed to be an order of magnitude lower than the vapor volume derivative. The minus sign shows that a vapor structure is considered aggressive only when the relative variation of its vapor volume is negative (condensation), thus giving a positive potential power value. The aggressiveness intensity is characterized then as

$$P_{pot}^{mat} = \eta^{**} P_{pot} \tag{3}$$

where η^{**} is the energy transfer efficiency and is a function of the hydrodynamic characteristics of the main flow (the reference velocity of the flow V_{ref}, and the cavitation number σ), the distance, and the angle between the collapse center and the material surface. This efficiency depends on the type, unsteadiness and geometry of the cavitating flow. However, it should be mentioned here that, from the definition of the potential power, a lot of information regarding the flow characteristics and cavitation development is already included. Consequently, the distance and the angle between the accumulated energy at the collapse center and the material surface seem to be the most important influential factors.

When the vapor structures collapse, the emitted pressure waves apply a pressure wave power on the surface that is defined as

$$P_{waves}^{mat} = \eta^* P_{pot}^{mat} \tag{4}$$

where the collapse efficiency η^* characterizes the aggressiveness power of the vapor/gas implosion. It depends mainly on the initial vapor volume, which is a function of the initial bubble radius R_0, the initial gas pressure p_{g_0} within the bubble, and the surrounding pressure p_∞. The plastic deformation due to the pressure waves (during the incubation period) is characterized by the deformed volume V_{pit}. Therefore, the pressure wave power density is obtained as follows:

$$\frac{P_{waves}^{mat}}{\Delta S} = \beta \frac{\sum V_{pit}}{\Delta t \Delta S} = \beta V_d \tag{5}$$

where V_d is the volume damage rate, and β is a coefficient related to the surface material.

The main advantage of this model is that it follows a physical energy balance process. However, the applicability and reliability of this model depends strongly on the assessment of the two efficiencies η^{**} and η^*, and the material parameter β.

Regarding the energy transfer efficiency η^{**} Flageul et al. [30] proposed an empirical approximation for the distance to the solid h_{agr}, below which it is assumed that the vapor structures are close enough to be considered as aggressive. Based on Kato et al. [27] this distance, can be approximated as the 10% of the thickness of the sheet cavity. Nevertheless, it is not only the distance that determines the aggressiveness of the structures, but also the angle of the structures to the surface. Thus, Leclercq et al. [24] used the solid angle approach to account for both the distance and the angle dependencies, to calculate the "instantaneous cavitation intensity" P_{pot}^{mat}.

A rather physical explanation of this "instantaneous cavitation intensity" could be the maximum aggressiveness of an initial vapor cloud, for a certain amount of potential energy within the cloud, and a specified collapse time. In other words, it is assumed that the whole potential energy is converted into a shock wave, neglecting any rebound effects and any heat transfer to the surrounding liquid.

2.2 Erosion Model 2. This model by Dular and Coutier-Delgosha [28] is based on the microjet formation. Single bubbles, present near the solid surface, start to oscillate due to shock waves, traveling toward the surface, generated by the collapse of vapor clouds. Because of the oscillations of the single bubbles, a high-velocity liquid jet impact can occur, causing damage on the surface. It is stated that, the eroded surface is a result of repetition of the phenomenon mentioned above, considering only the incubation period. According to this erosion risk model the local velocity of the microjet is one of the most critical quantities for the prediction of cavitation erosion. The jet velocity is determined by Plesset and Chapman [1] as

$$u_{jet} = 8.97\gamma^2 \sqrt{\frac{p - p_v}{\rho}} \tag{6}$$

where γ is the nondimensional distance from the bubble center to the surface ($\gamma = H/R_0$, where H is the distance and R_0 is the bubble radius), p is the reference pressure, p_v is the vapor pressure, and ρ is the liquid density. Based on the local velocity, the water hammer pressure can be expressed as

$$p_{hammer} \approx u_{jet} \rho_l c_l \tag{7}$$

where c_l is the speed of sound of pure liquid and ρ_l the liquid density. Assuming a perfectly rigid, solid surface, which behaves as a perfectly plastic solid, the critical velocity, for which the yield stress p_y is reached, can be expressed as derived by Lush [31]

$$u_{crit} \approx \sqrt{\frac{p_y}{\rho_l}\left(1 - \left(1 + \frac{p_y}{B}\right)^{\frac{-1}{n}}\right)} \tag{8}$$

where $B = 300$ MPa and $n = 7$ for liquid water.

While this hammer stress is definitely the most impressive impact, it is not clear whether it is the important damaging mechanism. Possibly, according to Plesset and Chapman [1], it is not the water hammer pressure that makes the jet potentially aggressive, because the water hammer incidence time is relatively small. The duration is estimated to be no longer than the time for the impact signal to traverse the radius of the jet. Then, it would rather be the stagnation pressure, established right after the water hammer pressure, that is responsible for pit formation, because its duration is an order of magnitude larger, while its amplitude can be of the same order (jet velocities have been reported to be even higher than 1000 m/s [32,33]). Nevertheless, this model does not consider the latter as a pressure pulse source.

To determine the erosion intensity from such an impact, Peters et al. [34] proposed a dimensionless intensity coefficient $c_{\text{intensity}}$, which relates the local jet velocity u_{jet} to the critical velocity u_{crit}, as well as the water hammer pressure p_{hammer} to the pressure needed to reach the limit, before which deformation starts to occur. It is defined as follows:

$$c_{\text{intensity}} = \frac{u_{\text{jet}}}{u_{\text{crit}}} \approx \frac{p_{\text{hammer}}}{p_{\text{plastic}}} \tag{9}$$

This coefficient expresses the erosion intensity of a single microjet impact on a face and it is calculated for every impact on a face of the desired surface. When there is no impact on a face the coefficient is equal to 0, while impacted faces have a value higher than 1, as the jet velocity in this case is higher than the critical velocity. Afterward, all the intensity coefficients are integrated over the whole time interval for every face, and then they are normalized by the total sum of $c_{\text{intensity}}$ in the whole domain. Thus, the deformation coefficient c_{def} is defined as

$$c_{\text{def}} = \frac{\sum_{t}^{T} c_{\text{intensity}}}{\sum_{n}^{N} \left(\sum_{t}^{T} c_{\text{intensity,t}} \right)_{n}} \tag{10}$$

where t is the time-step index, T the total calculation time, n the face index and N the total number of eroded faces. In the end, the value of the deformation coefficient c_{def} gives the fraction of the erosion on every face compared to the total predicted erosion.

It should be noted that the physical process assumed to be responsible for cavitation erosion in this model is based on the notion that damage is caused due to the impingement of the microjet, associated with the implosion of the individual bubbles, while in this paper, it is hypothesized that the acoustic power, released from this mechanism is significantly smaller than the acoustic power, that is released from a synchronized collapse of a bubbly cloud collapse. Moreover, a disadvantage of the model is that it accounts only for the plastic deformation of the surface (during the incubation period). Consequently, this model cannot be used to assess the actual damage rate but only the erosion risk.

2.3 Erosion Model 3—Collapse Detector. The concept of the "collapse detector" by Mihatsch et al. [29] involves the derivation of a set of physical criteria to detect the collapse of isolated clouds and to evaluate the strength of the generated shock waves. The definition of the collapse detector is given as follows:

- Computational cells where the vapor volume content condenses completely during the last time step are considered as "candidates." If the surrounding cells of a "candidate" contain liquid only, an isolated collapse is detected.
- Once a collapse is detected, the maximum pressure is generated at that instant in time, when the divergence of the velocity field changes its sign.
- The strength of the collapse is characterized by its maximum (negative) divergence and its maximum pressure.

The collapse detector offers two main advantages over just monitoring the maximum pressure. It automatically distinguishes the difference between the collapse maximum pressure and the high pressures due to stagnation points or wave interaction, and the number of collapse events, as well as their position, and their strength provide important information about a possible stress profile the material is exposed to. This information can be used to estimate erosion rates.

The main drawback of the collapse detector is the missing information of the collapse intensity on the material surface. To overcome this issue, Mihatsch et al. [29] proposed an efficient projection method. The final pressure impact on the wall, p_{wall} is obtained, using the linear decay law, from the maximum pressure at the collapse center p_{collapse}, the distance of the collapse from the wall r_{wall}, and the cube root of the cell volume V_{cell}, where the collapse was detected

$$p_{\text{wall}} \sim \frac{\sqrt[3]{V_{\text{cell}}}}{r_{\text{wall}}} p_{\text{collapse}} \tag{11}$$

The collapse detector is designed for a density based compressible solver, where the pressure at the collapse center can reliably be estimated, given that sufficient temporal resolution has been applied, and any grid dependencies have been taken care of. In an incompressible flow, the prediction of maximum pressure is not assured and it is very sensitive to grid and time-step resolution [35]. However, the number of the collapse events and their position can still provide very important information. Even though the collapse intensity may not be correctly predicted, multiple collapses around a specific area can indicate a high erosion risk. Furthermore, the detection of the candidate cell can be very useful for the reconstruction of the pressure driving the collapse. Thus, further investigation is needed, whether this model could be combined with other methods, suitable for pressure based incompressible solvers.

2.4 Evaluation of Models. The model by Dular and Delgoscha is based on the notion, that the damage is caused by the impingement of the liquid microjet, whereas in this paper we follow the hypothesis by Terwisga et al. [21], that a synchronized bubble collapse can release much higher acoustic power, than the microjet from a single bubble. Furthermore, it is not obvious whether the water hammer pressure, which is considered as the damage mechanism in this model, is the dominant source of damage, when a liquid jet is formed. The stagnation pressure may contribute more to the surface material loss. Although its magnitude is somewhat lower, its duration is an order of magnitude larger.

The models by Mihatsch et al. and Fortes-Patella et al., which are based on energy balance, are preferred for providing a more detailed physical basis. The model by Mihatsch et al., however, requires a reliable prediction of the maximum pressure, originated by the collapse of vapor structures, which may not be reliably predicted by an incompressible pressure based solver. Thus, the energy balance approach by Fortes-Patella et al. provides the best framework for erosion risk assessment using an incompressible pressure based URANS solver. The model used in this paper, described in Sec. 3.4, has its basis on this approach.

3 Numerical Modeling

3.1 Governing Equations. The Reynolds-averaged Navier–Stokes (RANS) equations are solved using the commercial solver STAR-CCM+, where each instantaneous quantity can be split into time-averaged and fluctuating components. The numerical simulations are based on finite volume method, and an incompressible segregated flow model is selected solving the integral conservation equations of mass and momentum in a sequential manner combined with the SIMPLE pressure–velocity coupling algorithm. For the time marching, a second-order implicit method is used, and for the convective terms, a second-order upwind

scheme is adopted. From the basic principles of conservation of mass and momentum, the governing equations are written as follows:

$$\frac{\partial \rho}{\partial t} + \nabla \cdot (\rho \mathbf{u}) = 0 \tag{12}$$

$$\frac{\partial (\rho \mathbf{u})}{\partial t} + \nabla \cdot (\rho \mathbf{u}\mathbf{u}) = -\nabla p + \rho f + \nabla \cdot \tau \tag{13}$$

where $\mathbf{u}$ is the velocity tensor, ρ is the fluid density, p the pressure, ρf the exterior force density per unit mass, and τ the viscous part of the stress tensor.

A homogeneous multiphase model is used, referred to as volume of fluid (VOF) in STAR-CCM+, treating the fluid as a single continuum with two phases, assuming a no-slip condition between liquid and vapor phase, with varying properties in space according to its composition a_v. The vapor phase is transported in order to compute the vapor volume fraction. The liquid volume fraction is determined from the condition:

$$a_v + a_l = 1 \tag{14}$$

while density and viscosity are defined, respectively, as

$$\rho = a_v \rho_v + a_l \rho_l \quad \text{and} \quad \mu = a_v \mu_v + a_l \mu_l \tag{15}$$

3.2 Turbulence Modeling. In this study the shear stress transport k–ω turbulence model, developed by Menter [36], is used (as result of previous study [37]). In order to fully resolve the boundary layer, the numerical mesh has been properly refined and a low-$y+$ wall treatment has been chosen. This approach effectively blends a k–ε model in the far field with a k–ω model near the wall. Reboud and Delannoy [38] showed the important role of the re-entrant jet on the cavity break-off cycle. However, the use of this turbulence model leads to very strong turbulent viscosity in the cavity wake hindering the re-entrant jet formation. It is stated by Reboud et al. [39], that this effect, which is not representative of the real behavior, has been analyzed to be related to the hypothesis of homogeneous flow and its no-slip condition between the two phases. That no-slip condition behaves as an artificial increase of dissipation.

That problem has been treated by an empirical reduction of turbulence dissipative terms in the two-phase regions, by modifying the turbulent viscosity [39]

$$\mu_t = f(\rho) C_\omega \frac{k}{\omega} \tag{16}$$

$$f(\rho) = \rho_v + \frac{(\rho_m - \rho_v)^n}{(\rho_l - \rho_v)^{(n-1)}}; \quad n \gg 1 \tag{17}$$

where ρ_v is the vapor density, ρ_l the liquid density, and ρ_m the mixture density. For the constant n a recommended value $n = 10$ has been used. With this modification, the turbulent viscosity is modified in phase transition regions, according to the density change. Therefore, the numerical simulations are improved by taking into account the influence of the local compressibility effects of the vapor/liquid mixture on the turbulent structure, which where not considered before by the common two equation turbulence models for incompressible RANS methods.

3.3 Cavitation Modeling. An additional conservation equation that describes the transport of vapor volume fraction α_ν is solved

$$\frac{\partial \alpha_\nu}{\partial t} + \nabla \cdot (\alpha_\nu \mathbf{u}) = S_{\alpha_\nu} \tag{18}$$

In Eq. (18), S_{α_ν} represents the source of volume fraction of vapor. In order to account for bubble growth and collapse, a cavitation model should be introduced for the source term of the volume fraction of vapor. The cavitation model used in this study is the model proposed by Schnerr and Sauer [40] based on a simplified Rayleigh–Plesset equation, which neglects the influence of bubble growth acceleration, as well as viscous and surface tension effects:

$$\frac{dR}{dt} = \text{sign}(p_\nu - p) \frac{\sqrt{2|p_\nu - p|}}{3\rho_l} \tag{19}$$

where p_ν is the saturation pressure, p is the local pressure around the bubble, and ρ_l is the fluid density. According to this rate, the source term in Eq. (18) is defined as

$$S_{\alpha_\nu} = \frac{4\pi R^2 n_0}{1 + \left(\frac{4}{3}\pi R^3\right) n_0} \frac{dR}{dt} \tag{20}$$

3.4 Cavitation Erosion Risk Assessment. According to the approach of Fortes-Patella et al. [23], as described in Sec. 2, pressure waves emitted during the collapses of vapor structures seem to be the main factor contributing to cavitation erosion. The potential energy of a cavity with volume V_ν is given by Eq. (1). It is interesting to note that, the model by Fortes-Patella et al. [23] defines the surrounding pressure (pressure driving the collapse) as the pressure at infinity, p_∞. This indicates, that the pressure driving the collapse is constant and equal to the pressure at infinity. Here, the driving pressure term is further on referred to as p_d, denoting a general unknown pressure field driving the collapse, assuming that the pressure, surrounding the cloud cavities, differs from the pressure at infinity. Then, the instantaneous potential power, as defined in Eq. (2), becomes

$$P_{\text{pot}} = (p_d - p_\nu) \cdot \frac{DV_\nu}{Dt} + \frac{Dp_d}{Dt} \cdot V_\nu \tag{21}$$

In Eq. (21) both derivatives are considered, and they represent Lagrangian time derivatives. Therefore, the potential power density can be estimated in every cell from

$$\frac{P_{\text{pot}}}{V_{\text{cell}}} = (p_d - p_\nu) \cdot \frac{D\alpha_\nu}{Dt} + \frac{Dp_d}{Dt} \cdot \alpha_\nu \tag{22}$$

where $\alpha_\nu = V_\nu / V_{\text{cell}}$ is the void fraction. Furthermore, the void fraction is defined as $\alpha_\nu = (\rho - \rho_l)/(\rho_\nu - \rho_l)$, and from the local mass conservation $\partial\rho/\partial t + \text{div}(\rho u) = 0$ the potential power density becomes [24,30]

$$\frac{P_{\text{pot}}}{V_{\text{cell}}} = (p_d - p_\nu) \cdot \frac{\rho}{\rho_l - \rho_\nu} \text{div}\mathbf{u} + \frac{\rho - \rho_l}{\rho_\nu - \rho_l} \left(\frac{\partial p_d}{\partial t} + \mathbf{u} \cdot \nabla p_d \right) \tag{23}$$

We assume that a change of energy in the domain, happens only when there is a change in the total vapor volume. Consequently, in this model, a vapor structure releases energy gradually as it condenses, and not instantaneously after its collapse. By looking the two terms of Eq. (23) separately, only the first term describes volume change. The second term describes the change in ambient conditions that a bubble is experiencing for constant volume. As a cavity structure travels toward a positive/negative pressure gradient, its potential energy will change. However, it has no effect on the collapse energy balance, as long as it does not experience any volume change. Thus, the second term from Eq. (23) should not be taken into account for the radiated energy. Furthermore, the effect of the pressure gradient on the energy release is depicted by the p_d term, as stated by Schenke and Terwisga [41]. Thus, the local impact rate $\dot{e}(t)$ is computed in every cell as follows:

$$\dot{e}(t) = -(p_d - p_\nu) \cdot \underbrace{\left(\frac{\partial \alpha}{\partial t} + u \cdot \nabla \alpha\right)}_{\frac{D\alpha}{Dt}} = -(p_d - p_\nu) \cdot \frac{\rho}{\rho_l - \rho_\nu} \text{div}\mathbf{u} \tag{24}$$

As it is shown in Eq. (24), in an Eulerian reference frame, the local impact rate $\dot{e}(t)$ can be calculated either by the material derivative of the vapor volume fraction or the velocity divergence. To account only for condensation, $D\alpha/Dt$ (or div$\mathbf{u}$) should be negative, and a minus sign is needed to give a positive energy release. In both cases, an unknown error is introduced. The advective term $u \cdot \nabla \alpha$ and the velocity divergence term on the left-hand side and the right-hand side of Eq. (24), respectively, cannot be computed directly, as after the discretization of the transport equation of the vapor volume, a combined term is computed, that includes the contribution of both terms. Thus, the divergence term cannot be separated from the advective term, and each one of them needs to be reconstructed. The reconstruction of these terms is responsible for the numerical error. Nevertheless, it is assumed that the advective term has a much smaller contribution to the volume change than the divergence term, allowing us to compute the local impact rate $\dot{e}(t)$ from the partial derivative of the vapor volume $\partial\alpha/\partial t$

$$\dot{e}(t) = -(p_d - p_\nu) \cdot \frac{\partial \alpha}{\partial t} = -(p_d - p_\nu) \cdot \left(\frac{\rho}{\rho_l - \rho_\nu} \text{div}\mathbf{u} - u \cdot \nabla \alpha\right) \tag{25}$$

Assuming that each point source emits its potential energy as a radial wave of infinitely large propagation speed, Leclercq et al. [24] define the potential power impact on the material surface $\dot{e}_S(t)$ using an algebraic approximation, which is based on the solid angle projection on a planar triangle. Schenke and Terwisga [25] proposed a continuous form of the energy impact rate on a surface location. In the present work, it is hypothesized that the vapor structures, which are in contact with the surface, are much more aggressive than any other structure, in further distance from the wall. This hypothesis is based on the work of Phillip and Lauterborn [10], where they demonstrated that the largest erosive force is caused by the collapse of bubbles in direct contact with the boundary. Thus, we assume that the impact from the structures in direct contact with the surface, is much higher than any impact from any other structure away from the surface. Therefore, it is not required to calculate the distance and the projection of any vapor structure, adding no further computational cost. The local impact power is evaluated only on the first prism layer, and the surface face value is obtained. The velocity in those cells is practically zero, thus the advective term, emerging on the right hand side of Eq. (25) can be considered negligible, while the velocity divergence not necessarily, due to the finite volume formulation. This gives an extra credit to our assumption, that the condensation process is dominant, and the advective term has a much smaller contribution to the volume change. The local surface impact rate $\dot{e}_S(t)$ is then computed from the partial derivative of the vapor volume fraction $\partial\alpha/\partial t$, minimizing the numerical error. However, this needs further investigation.

The ambient pressure field, p_d, effectively driving the cavity collapse, introduces the largest uncertainty in the erosion risk assessment. The determination of this quantity is not straightforward for complex flow conditions. The local instantaneous cell pressure cannot be used as an estimate for the driving pressure, as the driving pressure needs to be computed at the same location where energy is radiated. There, the local pressure is almost equal to the vapor pressure, leading to a driving pressure difference $p_d - p_\nu$ close to zero. This is also depicted by the density-pressure trajectory, which should be very close to vapor pressure during phase change. On top of that, the driving pressure is practically never exactly constant in space [41]. In this study, the time-averaged pressure field is computed, from the instantaneous pressure field p_i in cavitating flow conditions, assuming this field to be the ambient pressure field driving the cavity collapses. This field is steady, and it is computed in the whole domain before the erosion risk assessment. In this way, we can at least get a rough estimate of the conditions that collapsing cavities experience on statistical average [25,37].

To address the cavitation erosion risk on the surface (since the local surface impact rate $\dot{e}_S(t)$ is known), two aggressiveness indicators are used as proposed by Schenke and Terwisga [25]:

$$\langle \dot{e}_S \rangle_{e_S} = \left(\frac{1}{e_S} \int_0^t \dot{e}_S^{n+1} dt\right)^{1/n} \tag{26}$$

and

$$\langle \dot{e}_S \rangle_f = \left(\frac{1}{T} \int_0^t \dot{e}_S^{n+1} dt\right)^{1/(n+1)} \tag{27}$$

where

$$e_S = \int_0^t \dot{e}_S dt \tag{28}$$

The indicator $\langle \dot{e}_S \rangle_{e_S}$ averages the local energy impact rate over the surface accumulated energy e_S, amplifying the local extreme events, and being independent from the impact frequency. On the other hand, the indicator $\langle \dot{e}_S \rangle_f$ is normalized by the total impact time T. It is proportional to the frequency of the impact, showing converging behavior as the impact time $T \to \infty$ [25]. The parameter n is used to emphasize the peak events. The indicators work as a generalized mean value (also known as power mean or Hölder mean). Each mean value lies between the smallest and the largest impacts, and it gets closer to the largest impacts, as the n parameter increases, converging to the maximum peak value as $n \to \infty$.

To allow a fair qualitative comparison between the indicators for different values of the n parameter, we further normalize each indicator by the maximum aggressiveness indication on the surface, for each parameter n

$$\langle \dot{e}_S \rangle'_{e_S} = \frac{\left(\frac{1}{e_S} \int_0^t \dot{e}_S^{n+1} dt\right)^{1/n}}{\max\left(\langle \dot{e}_S \rangle_{e_{S,n}}\right)} \tag{29}$$

and

$$\langle \dot{e}_S \rangle'_f = \frac{\left(\frac{1}{T} \int_0^t \dot{e}_S^{n+1} dt\right)^{1/(n+1)}}{\max\left(\langle \dot{e}_S \rangle_{f,n}\right)} \tag{30}$$

By using this feature scaling, we bring each indicator into the range [0,1]. Thus, we can easier identify the areas with high erosion risk and better analyze the whole impact distribution on the surface.

4 Test Case

The simulated hydrofoil is the Delft Twist 11 hydrofoil (Fig. 2). The section of the foil is a NACA 0009 hydrofoil with an angle of incidence that changes along the spanwise direction

$$a(\bar{y}) = a_{\max}(2|\bar{y} - 1|^3 - 3(\bar{y} - 1)^2 + 1) + a_{\text{wall}} \tag{31}$$

where $a_{\max} = 11$ deg the maximum angle of attack at the midspan, $\bar{y}$ is nondimensionalized with the chord length c and varies over

Fig. 2 Geometry of the Delft Twist 11 hydrofoil

the spanwidth $(0 \leq \bar{y} \leq 2)$ with $\bar{y} = 0$ at the wall. The chord length and the spanwise length are 150 mm and 300 mm, respectively. The twisted design and the larger angle of attack in the middle area cause the cavitation to mainly develop near the midspan.

The hydrofoil is simulated in wetted flow ($u_{in} = 6.75$ m/s, $P_{out} = 97$ kPa) and cavitating flow ($u_{in} = 6.97$ m/s, $\sigma = 1.07$) in -2 deg angle of incidence and water temperature 24 °C. A no-slip condition is applied on the foil and slip condition on the walls, as no cavitation development is expected near the tunnel walls. A symmetry plane is used at the midspan to reduce the computational cost. Figure 3 shows the computational domain and the imposed boundary conditions.

For the grid generation, trimmed hexahedral cells are used with local refinements and prism layers along the wall, with such first cell distance so the average $y+$ value is well below 1 to resolve the viscous sublayer. Several refinement levels are applied (Fig. 4). To ensure the geometrical similarity on the meshes for the assessment of numerical uncertainty, the following approach was used for the prism layer mesh, proposed by Crepier [42]:

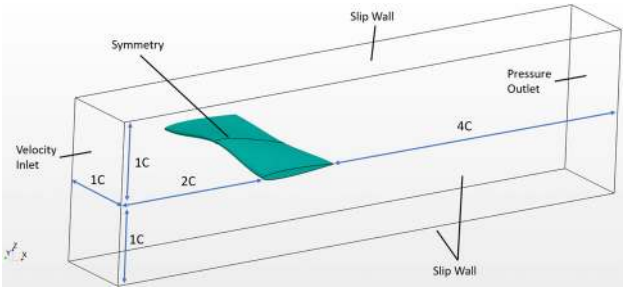

Fig. 3 Description of the computational domain and the boundary conditions

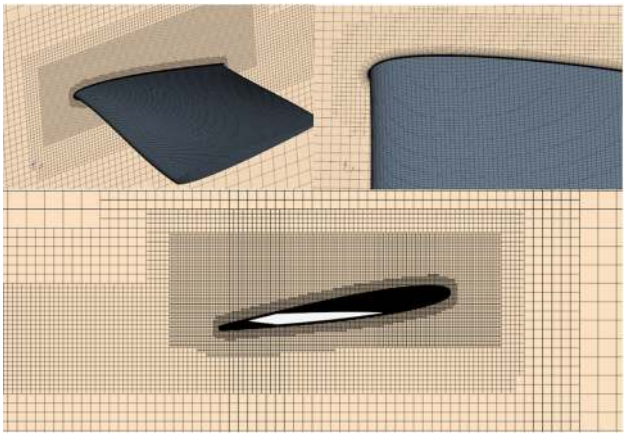

Fig. 4 Grid refinement levels around the foil

$$S_n = S_0 \frac{1 - r_1^{1/n}}{1 - r_1} \quad \text{and} \quad r_n = r_1^{1/n} \tag{32}$$

where S_0, r_1 the first cell size and the growth ratio of the initial coarse grid, respectively, and S_n, r_n the first cell size and the growth ratio of the grid refinement n ($n = 1$ for the coarse grid).

The analysis for the erosion risk assessment is carried out under different flow conditions, and a slightly smaller foil geometry, so that we are in line with the experiment by Cao et al. [26]. The inflow is 14 m/s, at 0 deg angle of incidence at the wall and 11 deg at the midchord, and a cavitation number $\sigma = 1.2$, resulting in an ambient pressure of about 120 kPa. The chord length and the spanwise length are 112.5 mm and 225 mm, respectively. The identified erosion regions, after the 3h paint test, are compared with our predicted impact distributions, obtained with the two aggressiveness indicators.

5 Results

A verification and validation study is conducted in wetted and cavitating flow. An extensive grid and time-step size sensitivity study is presented in Sec. 5.1, showing an impression of the uncertainty estimates. The results are validated against experimental data. Finally, the cavitation erosion risk is assessed and compared with the obtained impact distribution from paint test [26] (Sec. 5.2).

5.1 Verification and Validation

5.1.1 Wetted Flow. The results for the lift coefficient and the pressure distribution in wetted flow are presented and compared with experimental data. The Validation & Verification tool, developed by MARIN,[4] has been used to assess the numerical uncertainty. The analysis is based on the procedure given by Eca and Hoekstra [43]. Table 1 shows the lift force, for different grid densities. The deviation from the experimental value ($L_{\text{exp}} = 455$ N) is less than 4% for all the grids.

Figure 5 shows the convergence of the lift force with the grid refinement ratio h_i/h_1 (where h_i and h_1 the typical cell size of each grid and the finest grid, respectively), and the uncertainty estimates. The corresponding numerical uncertainty is indicated by an interval that contains the exact solution with 95% coverage. The observed order of convergence is equal to the theoretical one ($P = 2$), resulting in a low uncertainty for all grids (1.4% for the coarsest grid and 0.2% for the finest grid). The difference between the computed lift force and the measurements is higher than the numerical uncertainty in any of the cases. Nevertheless, the experimental uncertainty has been reported to be significantly high [44]. By assuming an uncertainty as low as 3%, the results for each grid density is within the acceptable range (Fig. 5).

The pressure distribution is also calculated in three different planes along the chord of the foil and is compared with experimental data. Two experimental datasets are available, from two different cavitation tunnels. The first dataset has been obtained at the Delft University of Technology, and the second one at the École Polytechnique Fédérale de Lausanne (EPFL). The test section of the cavitation tunnel in Delft is twice as big as the test section in Lausanne. The dimensions of our numerical "tunnel" are identical to the ones of the Delft cavitation tunnel, with only difference an extension downstream of the foil, to avoid interaction of the flow with the outlet boundary. Figure 6 shows the planes where the pressure distribution is measured, and Figs. 7–9 show the comparison between the different grid densities and the experimental results at each plane. A small sensitivity to the grid density is observed for the pressure at the leading and trailing edge, although it is negligible. A very good agreement is obtained with the EPFL measurements. The Delft measurements show

[4] http://www.refresco.org/verification-validation/utilitiesvv-tools/

Table 1 Number of cells, grid refinement ratio, average y^+ value, lift force and its numerical uncertainty for each grid

Grid	# Cells (10^6)	h_i/h_1	$\bar{y}^+$	Lift (N)	U (%)
G1	0.59	2.5	0.79	438	1.41
G2	1.05	2	0.63	439.8	0.9
G3	2.07	1.6	0.49	440	0.79
G4	4.17	1.2	0.37	442.6	0.5
G5	7.08	1	0.34	442.2	0.23

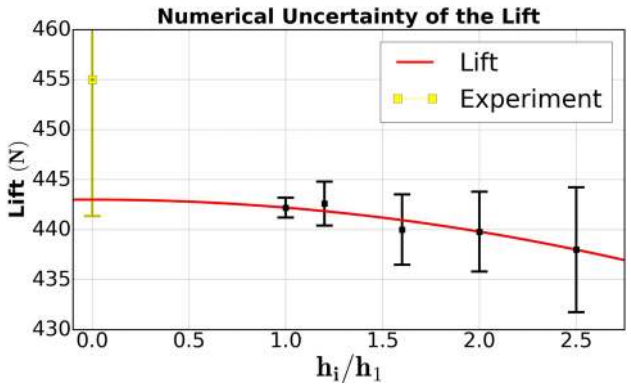

Fig. 5 Convergence of the lift force with the grid refinement ratio. Impression of the numerical uncertainty estimates.

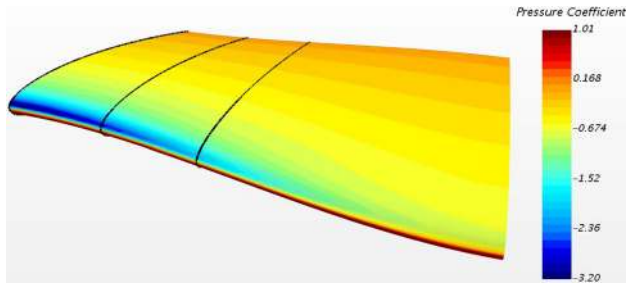

Fig. 6 The different planes where the pressure distribution is compared with experimental data

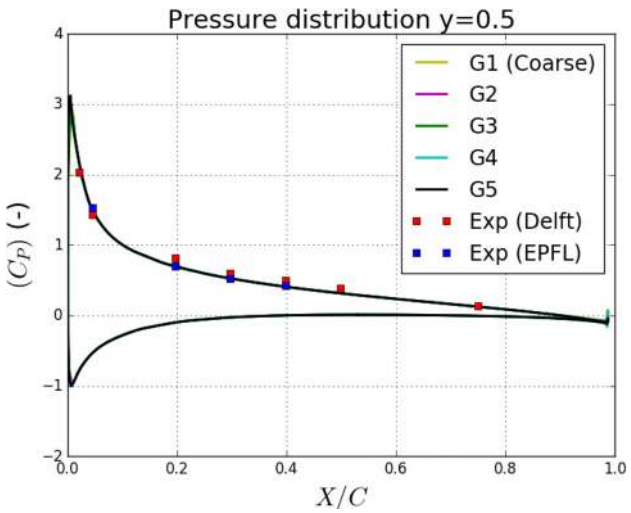

Fig. 7 Pressure distribution at the 50% of the span

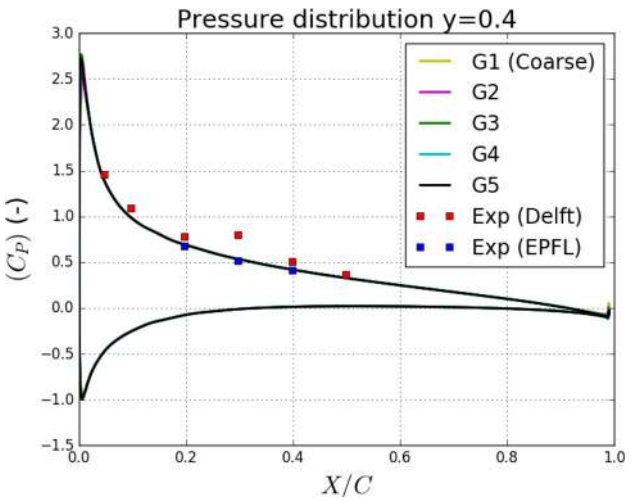

Fig. 8 Pressure distribution at the 40% of the span

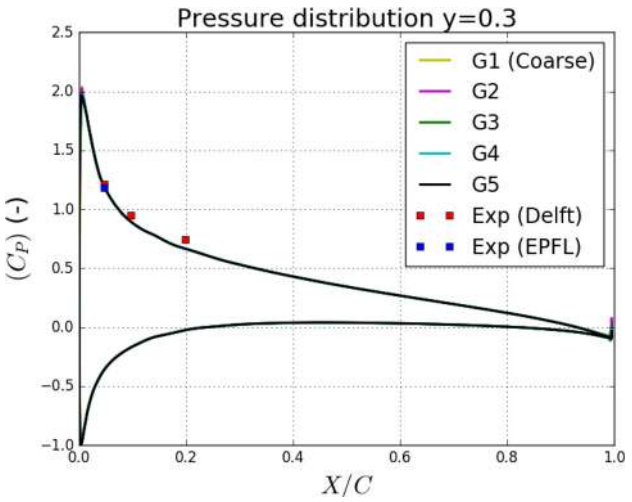

Fig. 9 Pressure distribution at the 30% of the span

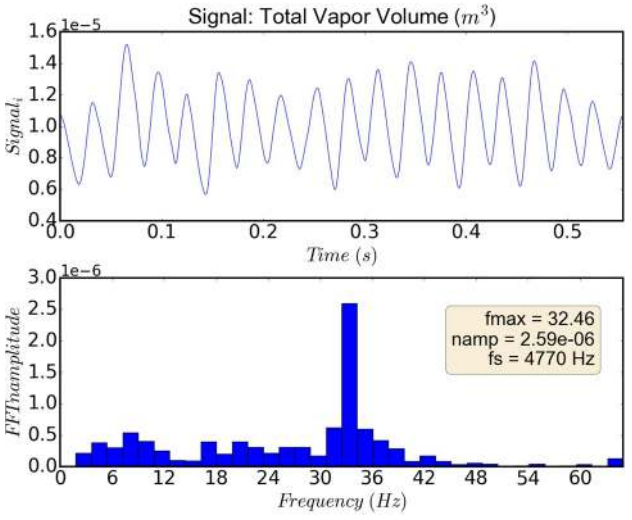

Fig. 10 Time history of the total vapor volume (top) and its spectral analysis (bottom)

somewhat higher pressure in the area between the 10% of the chord and the midchord. However, the difference is small enough to assume that the numerical results lie within the experimental uncertainty.

5.1.2 Cavitating Flow. The hydrofoil is tested in cavitating flow, for four different meshes (G1–G4 from Table 1) and five different time-step sizes. The time-step size is chosen by selecting the number of time-steps during a collapse. The collapse time of a shedded cloud can be calculated from the analytical solution of the Rayleigh-Plesset equation by just estimating the radius of the cloud

$$T_C^2 = \frac{\left(\xi^2 R_0 \rho\right)}{p} \tag{33}$$

where $\xi = 0.915$ is the Rayleigh factor, ρ the liquid density, p the far-field pressure and R_0 the bubbly cloud radius. By estimating the collapse time, we can determine in advance the number of time-steps during the collapse and therefore the time-step size for each computation. The number of time-steps is selected for the coarsest grid, assuming an average cloud radius of 1 mm. This number is chosen arbitrarily, as it is just an initial indication. We just consider a radius, that is much smaller than the size of the largest structures observed in the experiment. The final time-step size is determined by the uncertainty assessment. For the rest, the time-step size is computed so that a reference Courant Number remains constant. The reference Courant Number is defined as

$$\mathrm{CFL}_{\mathrm{ref}} = \frac{u_{\mathrm{in}} \Delta t}{\Delta x} \tag{34}$$

where u_{in} is the inflow velocity, Δt is the time-step, and Δx is the length of the smallest typical cell in x-direction.

The shedding frequency is derived from a fast Fourier analysis of the total vapor volume history (Fig. 10), and the pressure signal (Fig. 11) on the observation point P1 shown in Fig. 12. To make sure that both signals are stationary, and to quantify the statistical uncertainty, the transient scanning technique (TST) has been used [45,46]. The TST is a practical tool, developed within MARIN, to verify whether the mean value is constant or not, by locating trends in signals, at the beginning or at the end of the series. For CFD simulations, we only have to make sure that the end solution does not depend on the start solution anymore. There are two methods to estimate the statistical uncertainty, the autocovariance method and the segment method (for more information see

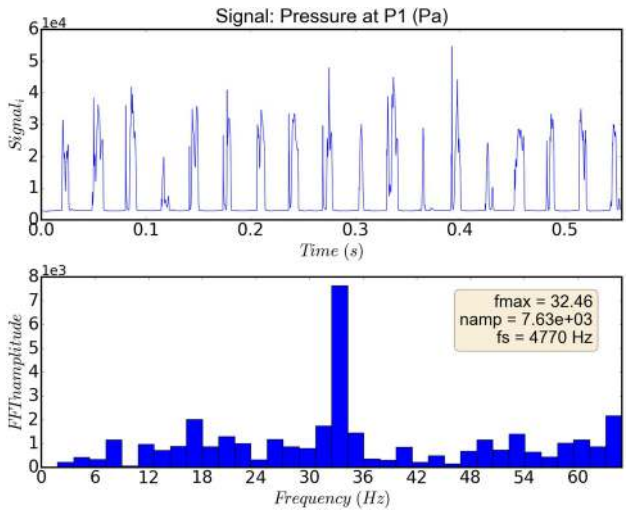

Fig. 11 Time history of the pressure at the observation point P1 (top) and its spectral analysis (bottom)

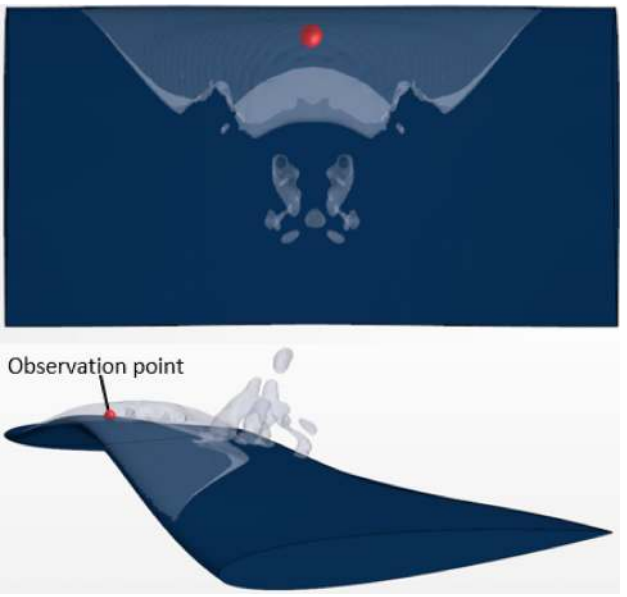

Fig. 12 Observation point P1, close to the surface

Ref. [45]). Both methods provide an estimate for the standard deviation of the mean s_m, called u_1, the standard uncertainty of the mean. In this study, we use the autocovariance method, therefore, u_1 is calculated as follows:

$$u_1 = \sqrt{\frac{1}{T}\int_0^T \left(1 - \frac{\tau}{T}\right) C_{xx,\mathrm{biased}}(\tau) d\tau} \tag{35}$$

where $C_{xx,\mathrm{biased}}(\tau)$ is the biased estimator for the autocovariance [45]. Using the TST based on cumulative u_1 calculated from the end of the signal, we can identify any start-up effect. For the signal to be stationary, u_1 should decay with the inverse of T, without showing any sudden rise ("hockey stick" [46]). Figures 13 and Fig. 14 show the cumulative u_1, nondimensionalized with the standard deviation of the process σ_i, in function with the section size T, for the total vapor volume, and the pressure signal on the observation point P1, respectively. A statistical uncertainty lower than 3% has been reached for the total vapor volume and lower than 1.5% for the pressure signal.

The numerical uncertainty is assessed in the same way as for the wetted flow condition. The results are shown in Figs. 15–17, where the convergence of the shedding frequency, the lift and the drag force with respect to the grid refinement ratio h_i/h_1 is

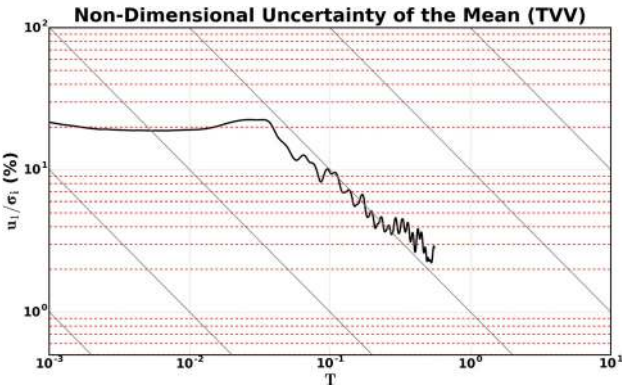

Fig. 13 TST results for the total vapor volume, after removing a section at the beginning

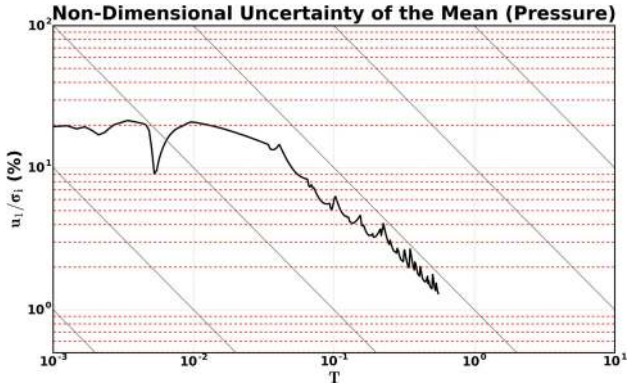

Fig. 14 TST results for the pressure signal at the observation point P1, after removing a section at the beginning

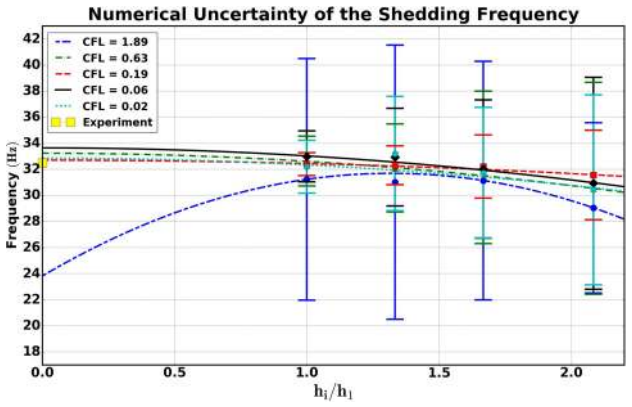

Fig. 15 Convergence of the shedding frequency with the grid refinement ratio. Impression of the numerical uncertainty estimates for different reference courant numbers.

indicated. For the shedding frequency, although some data points fairly deviate from the least square fit (scatter), especially for G3 ($h_i = 1.33$), the order of convergence reaches the theoretical one for CFL_{ref} below 1, giving an estimate of the exact solution between 32 and 34 Hz. An uncertainty of around 6% is achieved for CFL_{ref} below 1, apart from $CFL_{ref} = 0.19$, where the uncertainty drops below 3%. A good agreement is achieved with the experimentally obtained frequency, as well as other numerical studies (Table 2).

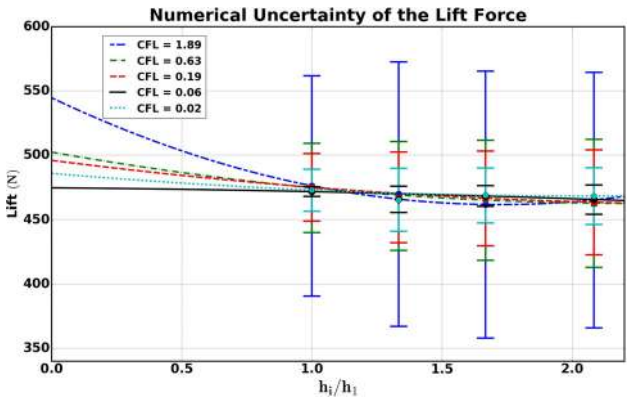

Fig. 16 Convergence of the lift force with the grid refinement ratio. Impression of the numerical uncertainty estimates for different reference courant numbers.

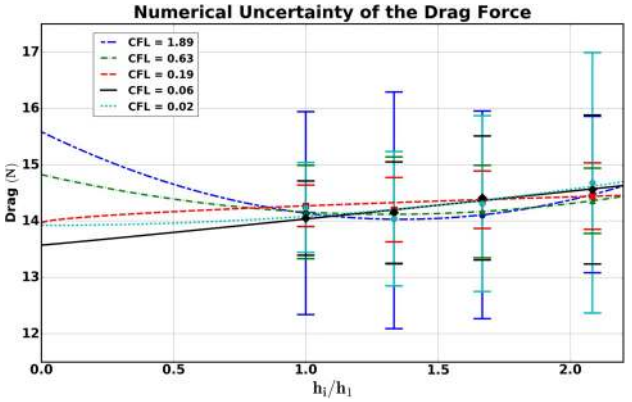

Fig. 17 Convergence of the drag force with the grid refinement ratio. Impression of the numerical uncertainty estimates for different reference courant numbers.

For the lift force, the order of convergence is not approaching the theoretical one. The same for the drag force, apart from the smallest time-step size. There are two main reasons for that. First, the coarse mesh (G1) might be too coarse that should have been excluded from the fit. In that case, an even finer mesh should be used. Second, the grids are not totally geometrically similar, increasing the chance of scatter in the results. However, the uncertainty is even lower than the one for the shedding frequency. For the lift force the discretization error is below 4% for $CFL_{ref} = 0.02$, and even below 1% for $CFL_{ref} = 0.06$. For the drag force, the uncertainty is around 6% for CFL_{ref} below 1, except for $CFL_{ref} = 0.19$, where the uncertainty is less than 3%.

Table 2 Comparison between the computed shedding frequency and the experimental frequency, as well as the frequency obtained from other numerical studies

Reference	Shedding frequency (Hz)
Foeth (experiment) [47]	32.55
Oprea [48]	31
Muzaferija et al. [49]	32
Vaz et. al. [44]	32.5
Current study	≈32.46

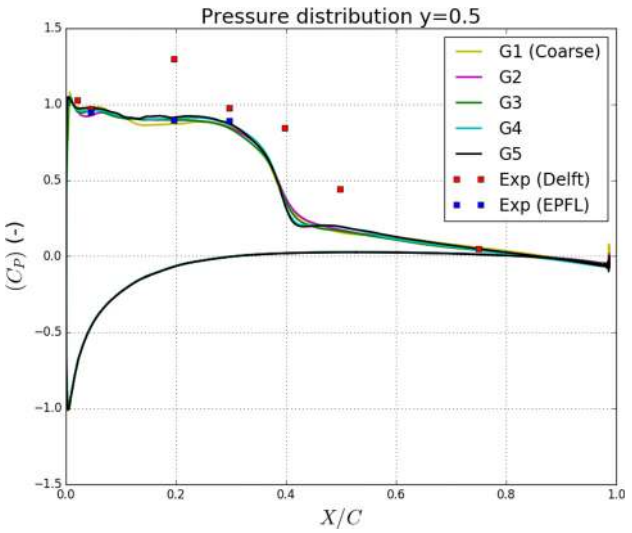

Fig. 18 Time-averaged pressure distribution at the midspan for different grid densities. Comparison with experimental measurements.

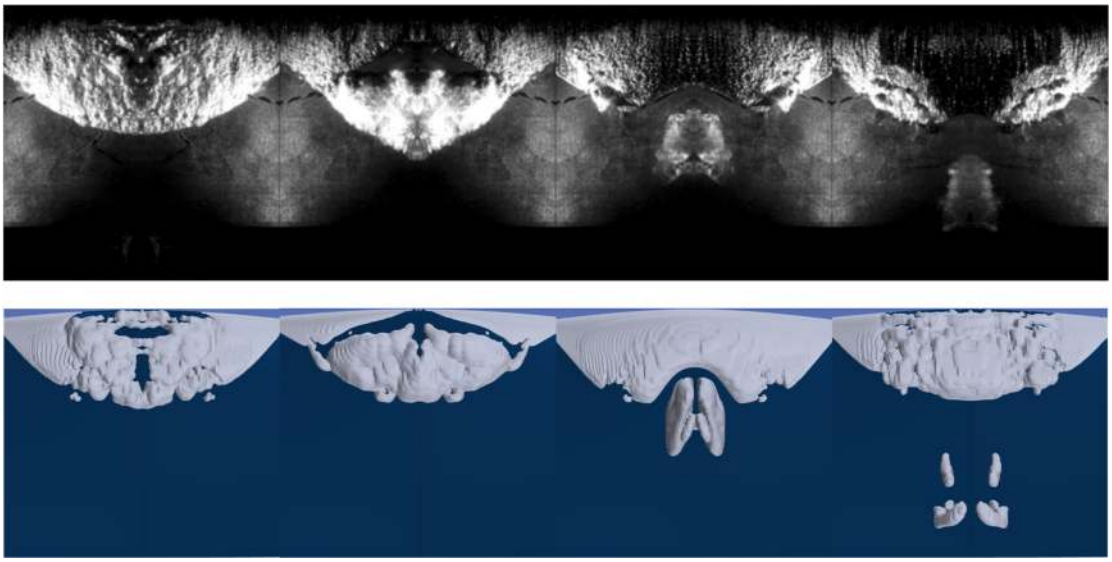

Fig. 19 Qualitative comparison between the particle image velocimetry imaging and the simulated shedding cycle, visualized as an isosurface of $a_v = 0.01$

Furthermore, the time-averaged pressure distribution at the midspan (Fig. 18) is also compared with experimental measurements. The results are insensitive to grid and time-step resolution. They agree well with the pressure data from EPFL, but they deviate from the data from TU Delft, underestimating the length of the sheet cavity (Fig. 18). The qualitative comparison between the shedding cycle from the particle image velocimetry imaging and the computations, visualized as an isosurface of $a_v = 0.01$ (see Fig. 19), shows similar behavior. Although a good agreement with the shedding frequency is obtained, we observe a slightly smaller sheet cavity length. Nevertheless, both the experimental and numerical observations are instantaneous snapshots of one shedding cycle, while the shedding process is a random process with variable vapor volume in each cycle.

5.2 Cavitation Erosion Risk. From the grid and time-step sensitivity study in Sec. 5.1, the finest grid (Grid 4 in Table 1) is used for the erosion risk prediction and the chosen time-step corresponds to $\mathrm{CFL}_{\mathrm{ref}} = 0.19$ $(dt = 6.1e-06s)$. First, we estimate cavitation aggressiveness, on the foil surface, for five different inflow velocities at the same cavitation number. The surface potential power density $P_{\mathrm{pot}}/\Delta S$ is computed, for each velocity, as the total accumulated energy on the surface E_S, divided by the sample time T and the surface area ΔS. Flow aggressiveness potential power density increases approximately as $P_{\mathrm{pot}} \sim u_{\mathrm{in}}^{3.2}$ (see Fig. 20) showing a similar trend with experiments [16], as well as other numerical studies [24,50].

The time-averaged pressure field $\bar{p}_t$ is computed from the local instantaneous pressure field p_i, under cavitating flow conditions, assuming this field to be the ambient pressure field driving the collapses. Figure 21 shows the evolution of both signals in time, at the observation point P1. After $\bar{p}_t$ has converged in each volume cell, a distinct pressure recovery region is distinct (Fig. 22), compared to the instantaneous pressure field (Fig. 23).

Figure 24 depicts the distribution of the accumulated surface energy e_s, when (a) the instantaneous pressure p_i or (b) the time-averaged pressure $\bar{p}_t$ is used as the driving pressure. When the instantaneous pressure field is driving the collapses, we would expect that the energy accumulated on the surface is negligible, as the instantaneous pressure in areas where phase transition occurs should be equal to vapor pressure (see also Sec. 3.4). However, as a matter of fact, the driving pressure difference $p_d - p_v$ is not close to zero, resulting in accumulation of collapse energy close to the leading edge. Similar trend has been found by Li and Terwisga [51], where they also used the instantaneous local pressure as driving pressure, and inevitably predicted high impact rates close to the leading edge. Nevertheless, the nonzero driving pressure difference may be considered as a numerical artifact, due to the

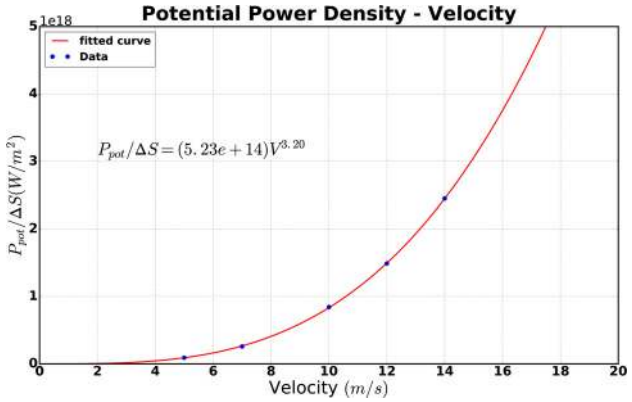

Fig. 20 Flow aggressiveness potential power density, as a function of the flow velocity

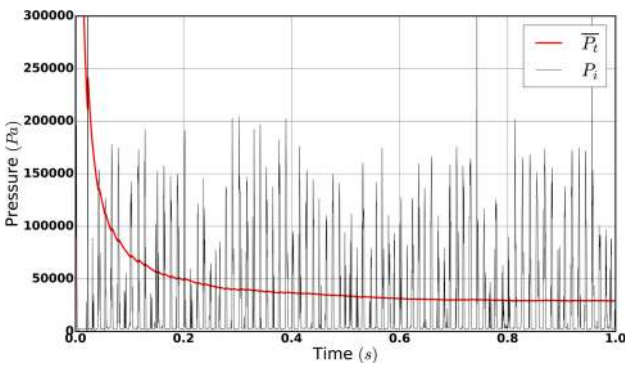

Fig. 21 Pressure signal and the time-averaged pressure evolution at the observation point

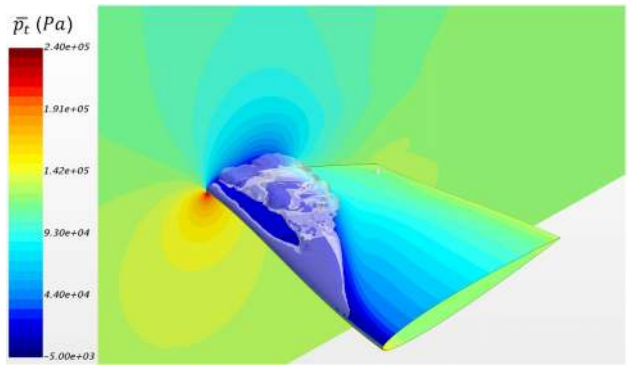

Fig. 22 Time-averaged pressure field $\bar{p}_t$ after it has converged in each volume cell, showing a distinct pressure recovery region

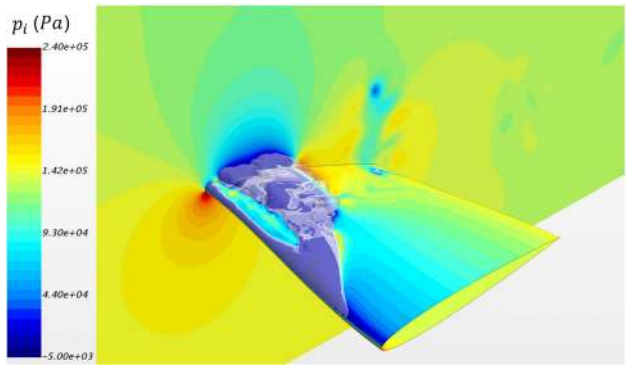

Fig. 23 Instantaneous pressure field p_i for a random instant of time

cavitation modeling approach. It strongly depends on the mass transfer source term and the evolution of the density-pressure trajectory. The closer it gets to the vapor pressure during phase change, the smaller the driving pressure difference, and therefore the accumulated surface energy. On the other hand, when we account for the effect of spatial pressure recovery, large impact rates emerge toward the trailing edge region (Fig. 24(*b*)).

The rapidness of the local impacts is assessed by the two aggressiveness indicators $\langle \dot{e}_S \rangle_f$ and $\langle \dot{e}_S \rangle_{e_S}$ given by Eq. (26). Both indicators have been tested for different n values (see Fig. 25). Indicator $\langle \dot{e}_S \rangle_f$ seems to be more sensitive to the n parameter, showing different impact distributions for different n values. Low n, results in large impact rates at the leading edge, which are getting lower as the n increases, resulting in larger predicted impact rates toward the trailing edge, with similar magnitude. Indicator $\langle \dot{e}_S \rangle_{e_S}$ is less sensitive to the n constant, showing similar impact distributions for different n values, however with larger magnitude for higher n values. Qualitatively, both indicators show similar aggressiveness distribution for high n values. The high erosion risk regions on the surface show a good qualitative agreement with the damage pattern obtained by Cao [26] in Fig. 26. High erosion risk was predicted in all three regions, identified from experimental paint tests.

6 Conclusion

Cavitation erosion can cause severe damage to the propeller blades, and gives opposite design trends to fuel efficiency, rendering cavitation erosion risk assessment imperative, already in the design stage. Making an early stage propeller erosion assessment requires balance between sufficient numerical resolution and computational effort. In this study, the shock wave emission, originated by the collapse of cloudy vapor structures, is considered as the most aggressive mechanism for cavitation erosion. Therefore, a validation and verification study has been conducted on the ability of a URANS solver, treating the pure phases as incompressible, to predict those cavity structures and the consequent energy transfer to the surface of the Delft Twist 11 hydrofoil. The following conclusions are drawn:

- In wetted flow, the prediction of the lift force and the pressure distribution on the foil is in good agreement with the experimental measurements. The numerical uncertainty for the generated lift is lower than 1% for all mesh densities (apart from the coarsest grid).
- In the cavitating conditions, the shedding frequency converges with the grid refinement ratio, according to the theoretical order of convergence, and agrees well with the experimental frequency. The numerical uncertainty is somewhat higher than in wetted flow, however is less than 3% in the best case ($\mathrm{CFL}_{\mathrm{ref}} = 0.19$). The lift generated force does not converge with the grid refinement ratio, thus a finer mesh should be used for the uncertainty analysis. The same holds for the drag force, apart from the smallest time-step size, which follows the theoretical order of convergence. Nevertheless, the uncertainty estimates are quite low for the finer meshes (3% for the drag and even lower than 1% for the lift force).
- The flow aggressiveness in cavitating flow conditions has been estimated, following the energy balance approach proposed by Fortes-Patella et al. [16], and further elaborated by Flageul et al. [30], Leclercq et al. [24], and Schenke and van Terwisga [25]. We found that the cavitation aggressiveness potential power increases as $u_{\mathrm{in}}^{3.2}$, being in line with experimental [16] and other numerical results [24,50].
- The effect of the pressure field driving the collapse has been investigated. Accounting for special pressure recovery, by time averaging the local pressure field, strongly affects the distribution of the accumulated energy on the surface,

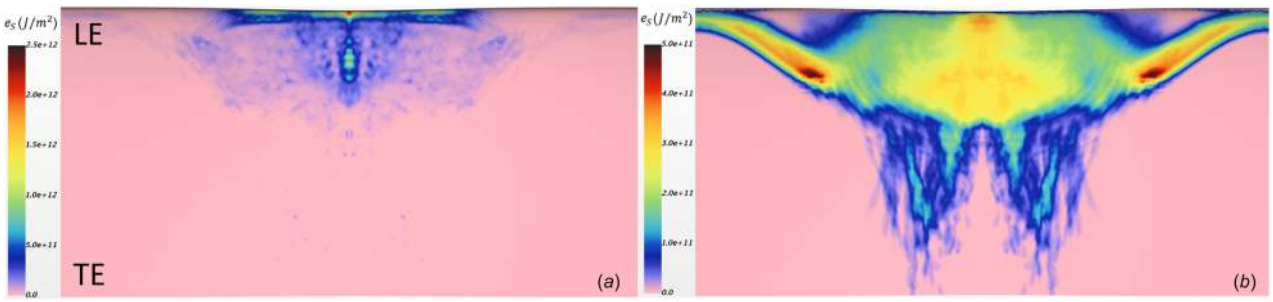

Fig. 24 Accumulated energy on the surface (*a*) for the instantaneous pressure field p_i and (*b*) the time-averaged pressure field $\bar{p}_t$

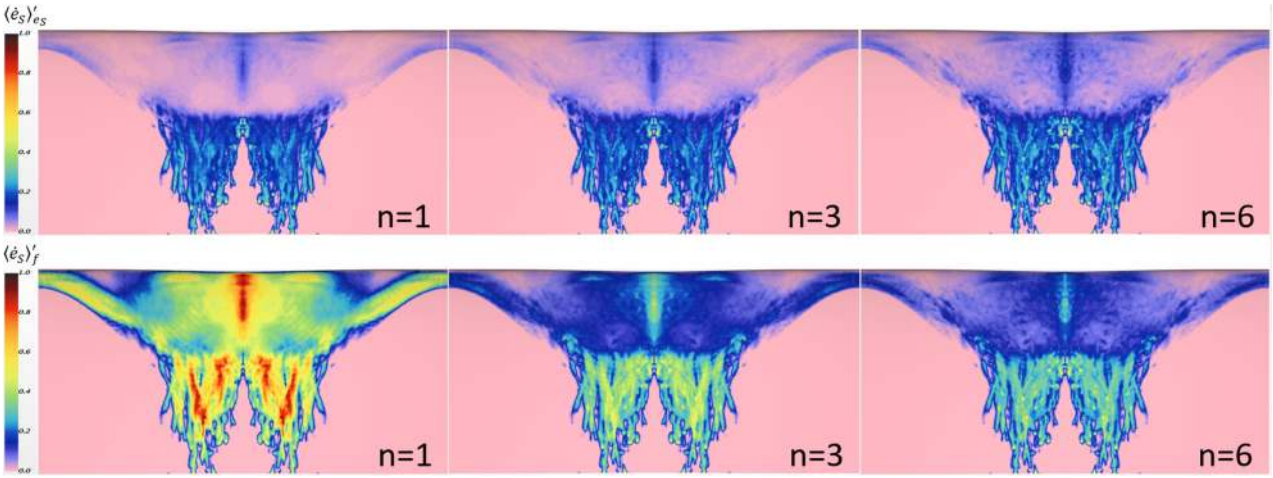

Fig. 25 Surface impact distribution for different values of the parameter *n*, for each aggressiveness indicator $\langle \dot{e}_S \rangle'_{es}$ (top) and $\langle \dot{e}_S \rangle'_f$ (bottom)

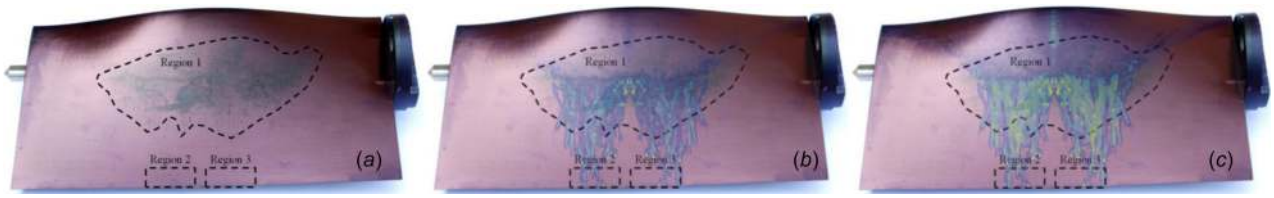

Fig. 26 Comparison between the surface impact distributions obtained from (*a*) 3 h of paint test, (*b*) the indicator $\langle \dot{e}_S \rangle'_{es}$, and (*c*) the indicator $\langle \dot{e}_S \rangle'_f$. The CFD solution, $n = 6$ for both indicators, has been plotted on the actual surface to compare the eroded regions with the paint test.

originated by the initial potential energy in the cavities. Next to that, the rapidness of the collapse event has been evaluated with two aggressiveness indicators. A parameter n is used to emphasize the peak events with higher amplitude. The indicator $\langle \dot{e}_S \rangle_f$ normalized by the total impact time, seems to be more sensitive to the n parameter. However, both indicators give similar impact distributions, when a high n value ($n = 6$), in combination with the time-averaged driving pressure field are used. The distributions agree well with the erosion pattern obtained from the paint test [26], indicating high erosion risk in all three identified regions.

7 Discussion

As a first assessment, our main hypothesis that the vapor structures, which are in contact with the surface, are much more aggressive than any other structure away from the surface (based on Ref. [10]) is initially confirmed. Our numerical model is able to predict high erosion risk in all three locations obtained from the paint test. However, some high risk was predicted also in the area in between of those regions, where no paint was removed in the experiment. This might be explained by the fact that in our model, energy is released instantaneously throughout the whole condensation process and not at the moment the cavity has collapsed. Thus, during the advection of the horseshoe cavity downstream, an impact is continuously computed, while the cavity condenses, leaving a footprint on the surface, before its final collapse close to the trailing edge. Apart from that, the water temperature during the experiment has not been reported, so the cavitating flow conditions might not be identical. Furthermore, it should be noted that the damage pattern from the paint test was obtained after 3 h, while the simulation time is only 0.7 s, probably not enough to obtain a fully converged impact distribution.

The contribution of vapor structures in further distance from the wall to the surface impact distribution, requires additional investigation in order to further confirm our main hypothesis. Moreover, the determination of the pressure effectively driving the collapse, still remains an issue and requires further research as well. We have shown that any change in the driving pressure term p_d, might have a considerable effect on the impact distribution. Therefore, more insight should be gained on the selection of the driving pressure. Yet, any attempt to estimate cavitation aggressiveness can only be related to a risk, as the material response has been left out of consideration in this paper.

Acknowledgment

This study was supported by the R&D Department of Wärtsilä Netherlands. Furthermore, we highly appreciate the valuable discussions with Sören Schenke at TU Delft and his feedback on the present work.

Funding Data

- H2020 Project CaFE ITN (Grant No. 642536; Funder ID: 10.13039/100010661).

Nomenclature

a = angle of incidence (deg)
B = 300 MPa for liquid water
c_{def} = deformation coefficient

$c_{\text{intensity}}$ = dimensionless erosion intensity coefficient
c_l = speed of sound of pure liquid (m/s)
$C_{xx,\text{biased}}(\tau)$ = biased estimator for the autocovariance
CFl_{ref} = reference Courant number
$\dot{e}(t)$ = local impact rate (W/m^3)
e_S = surface accumulated energy (J/m^2)
E_{pot} = initial potential energy inside a vapor structure (J)
$\dot{e_S}(t)$ = local surface impact rate (W/m^2)
$\langle \dot{e}_S \rangle'_{e_S}$ = aggressiveness indicator normalized by the accumulated energy e_S (W/m^2)
$\langle \dot{e}_S \rangle'_f$ = aggressiveness indicator normalized by the total impact time T (W/m^2)
H = distance from bubble center to the surface (m)
h_i = typical grid cell size
h_1 = typical cell size of the finest grid
k = turbulence kinetic energy
N = total number of eroded faces
n = face index
n = 7 for liquid water
n_0 = seed density (m^{-3})
p = reference pressure (N/m^2)
p_{collapse} = maximum pressure at collapse center (N/m^2)
p_d = pressure driving the collapse (N/m^2)
p_{hammer} = water hammer pressure (N/m^2)
p_i = instantaneous pressure field (N/m^2)
p_{out} = pressure at the outlet (N/m^2)
P_{pot} = instantaneous potential power (W)
p_ν = vapor pressure (N/m^2)
p_{wall} = pressure impact on the wall (N/m^2)
p_y = yield stress (N/m^2)
p_∞ = liquid pressure at infinity (N/m^2)
$\bar{p}_t$ = time-averaged pressure field (N/m^2)
$P_{\text{pot}}^{\text{mat}}$ = aggressiveness intensity (W)
$P_{\text{waves}}^{\text{mat}}$ = pressure wave power (W)
r_n = growth ratio of the grid with refinement ratio n
r_{wall} = distance of the collapse center from the wall (m)
R_0 = bubble radius (m)
r_1 = growth ratio of the coarse grid for $n = 1$
S_n = first cell size of the grid with refinement ratio n (m)
S_0 = first cell size of the coarse grid for $n = 1$ (m)
t = time step index (s)
T = total calculation/sample time (s)
T_c = collapse time (s)
$\mathbf{u}$ = velocity tensor
u_{crit} = critical velocity for which yield stress is reached (m/s)
u_{jet} = jet velocity (m/s)
u_{in} = inflow velocity (m/s)
u_1 = standard uncertainty of the mean
V_{cell} = cell volume (m^3)
V_d = volume damage rate (μm^3/mm^2/s)
V_{pit} = deformed volume (μm^3)
V_ν = vapor volume (m^3)
$\bar{y}$ = nondimensional span width
$\alpha_{\nu,l}$ = vapor and liquid volume fraction
β = mechanical characteristic coefficient (J/mm^3)
γ = nondimensional distance from the bubble center to the surface
ΔS = surface area (m^2)
Δt = time-step (s)
Δx = length of the smallest typical cell in x-direction (m)
η^* = collapse efficiency
η^{**} = hydrodynamic efficiency
μ = fluid dynamic viscosity (kg s/m^2)
$\mu_{t,\nu,l}$ = turbulent, vapor, and liquid dynamic viscosity (kg s/m^2)
ξ = 0.915 the Rayleigh factor
ρ = fluid density (kg/m^3)
$\rho_{\nu,l}$ = vapor and liquid density (kg/m^3)
τ = stress tensor
ω = specific dissipation rate of turbulent kinetic energy

References

[1] Plesset, M. S., and Chapman, R. B., 1971, "Collapse of an Initially Spherical Vapour Cavity in the Neighbourhood of a Solid Boundary," J. Fluid Mech., **47**(2), pp. 283–290.
[2] Rayleigh, L., 1917, "VIII. On the Pressure Developed in a Liquid During the Collapse of a Spherical Cavity," London, Edinburgh, Dublin Philos. Mag. J. Sci., **34**(200), pp. 94–98.
[3] Hickling, R., and Plesset, M. S., 1964, "Collapse and Rebound of a Spherical Bubble in Water," Phys. Fluids, **7**, pp. 7–14.
[4] Plesset, M. S., and Hsieh, D., 1977, "Theory of Gas Bubble Dynamics in Oscillating Pressure Fields," Phys. Fluids, **3**, pp. 882–892.
[5] Plesset, M. S., and Prosperetti, A., 1977, "Bubble Dynamics and Cavitation," Ann. Rev. Fluid Mech., **9**(1), pp. 145–185.
[6] Brennen, C. E., 1995, *Cavitation and Bubble Dynamics*, Oxford University Press, New York.
[7] van Wijngaarden, L., 1966, *On the Collective Collapse of a Large Number of Gas Bubbles in Water*, Netherlands Ship Model Basin, Wageningen, The Netherlands.
[8] Mørch, K. A., 1982, "Energy Considerations on the Collapse of Cavity Clusters," Appl. Sci. Res., **38**, p. 313.
[9] Isselin, J.-C., Alonclе, A.-P., and Autric, M., 1998, "On Laser Induced Single Bubble Near a Solid Boundary: Contribution to the Understanding of Erosion Phenomena," J. Appl. Phys., **84**(10), pp. 5766–5771.
[10] Philipp, A., and Lauterborn, W., 1998, "Cavitation Erosion by Single Laser-Produced Bubbles," J. Fluid Mech., **361**, pp. 75–116.
[11] Hammit, F. G., 1963, "Observations on Cavitation Damage in a Flowing System," J. Basic Eng., **85**(3), pp. 347–356.
[12] Vogel, A., and Lauterborn, W., 1988, "Acoustic Transient Generation by Laser-Produced Cavitation Bubbles Near Solid Boundaries," J. Acoust. Soc. Am., **84**(2), pp. 719–731.
[13] Dular, M., Stoffel, B., and Sirok, B., 2006, "Development of a Cavitation Erosion Model," Wear, **261**(5–6), pp. 642–655.
[14] Dular, M., Pozar, T., Zevnik, J., and Petkovsek, R., 2019, "High Speed Observation of Damage Created by a Collapse of a Single Cavitation Bubble," Wear, **418–419**, pp. 13–26.
[15] Fortes-Patella, R., and Reboud, J. L., 1998, "A New Approach to Evaluate the Cavitation Erosion Power," ASME J. Fluids Eng., **120**(2), pp. 335–344.
[16] Fortes-Patella, R., Challier, G., Reboud, J. L., and Archer, A., 2013, "Energy Balance in Cavitation Erosion: From Bubble Collapse to Indentation of Material Surface," ASME J. Fluids Eng., **135**(1), p. 011303.
[17] Franc, J. P., and Michel, J. M., 2004, *Fundamentals of Cavitation*, Kluwer Academic Publishers, Dordrecht, The Netherlands.
[18] Tomita, Y., and Shima, A., 1986, "Mechanisms of Impulsive Pressure Generation and Damage Pit Formation by Bubble Collapse," J. Fluid Mech., **169**(1), pp. 535–564.
[19] Bark, G., Berchiche, N., and Grekula, M., 2004, "Application of Principles for Observation and Analysis of Eroding Cavitation," *EROCAV Observation Handbook*, Chalmers University of Technology, Gothenburg, Sweeden.
[20] Tinguely, M., Obreschkow, D., Kobel, P., Dorsaz, N., de Bosset, A., and Farhat, M., 2012, "Energy Partition at the Collapse of Spherical Cavitation Bubbles," Phys. Rev. E, **86**(4 Pt 2), p. 046315.
[21] van Terwisga, T. J. C., Fitzsimmons, P. A., Li, Z., and Foeth, E. J., 2009, "Cavitation Erosion—A Review of Physical Mechanism and Erosion Risk Models," Seventh International Symposium on Cavitation, Ann Arbor, MI, Aug. 15–20, Paper No. 41.
[22] Eskilsson, C., and Bensow, R. E., 2015, "Estimation of Cavitation Erosion Intensity Using CFD: Numerical Comparison of Three Different Methods," Fourth International Symposium on Marine Propulsors, Austin, TX, Austin, TX, May 31–June 4, pp. 9–17.
[23] Fortes-Patella, R., Reboud, J.-L., and Briancon-Marjollet, L., 2004, "A Phenomenological and Numerical Model for Scaling the Flow Agressiveness in Cavitation Erosion," EROCAV Workshop, Val de Reuil, France, May.
[24] Leclercq, C., Archer, A., Fortes-Patella, R., and Cerru, F. R. F., 2017, "Numerical Cavitation Intensity on a Hydrofoil for 3D Homogeneous Unsteady Viscous Flows," Int. J. Fluid Mach. Syst., **10**(3), pp. 254–263.
[25] Schenke, S., and van Terwisga, T. J. C., 2018, "Erosive Aggressiveness of Collapsing Cavitating Structures," Tenth International Symposium on Cavitation, Baltimore, MD, May 14–16, Paper No. 69.
[26] Cao, Y. T., Peng, X. X., Yan, K., Xu, L. H., and Shu, L. W., 2017, "A Qualitative Study on the Relationship Between Cavitation Structure and Erosion Region Around a 3D Twisted Hydrofoil by Painting Method," Fifth International Symposium on Marine Propulsors, Espoo, Finland, June 12–15, pp. 1–5.
[27] Kato, H., Konno, A., Maeda, M., and Yamaguchi, H., 1996, "Possibility of Quantitative Prediction of Cavitation Erosion Without Model Test," ASME J. Fluids Eng., **118**(3), pp. 582–588.
[28] Dular, M., and Coutier-Delgosha, O., 2009, "Numerical Modelling of Cavitation Erosion," Int. J. Numer. Meth. Fluids, **61**(12), pp. 1388–1410.
[29] Mihatsch, M. S., Schmidt, S. J., Thalhamer, M., and Adams, N. A., 2011, "Numerical Prediction of Erosive Collapse Events in Unsteady Compressible Cavitating Flows," Fourth International Conference on Computational Methods in Marine Engineering, Lisbon, Portugal, Sept. 28–30, pp. 499–509.
[30] Flageul, C., Fortes-Patella, R., and Archer, A., 2012, "Cavitation Erosion Prediction by Numerical Simulations," 14th International Symposium on Transport

Phenomena and Dynamics of Rotating Machinery, Honolulu, HI, Feb. 27–Mar. 2.
[31] Lush, P., 1983, "Impact of a Liquid Mass on a Perfectly Plastic Solid," J. Fluid Mech., **135**(1), pp. 373–387.
[32] Lauer, E., Hu, X. Y., Hickel, S., and Adams, N. A., 2012, "Numerical Modelling and Investigation of Symmetric and Asymmetric Cavitation Bubble Dynamics," Comput. Fluids, **69**, pp. 1–19.
[33] Chahine, G. L., Franc, J.-P., and Karimi, A., eds., 2014, "Advanced Experimental and Numerical Techniques for Cavitation Erosion Prediction," *Cavitation and Cavitation Erosion: Computational and Experimental Approaches*, 1st. ed., Vol. 106, Springer, Dordrecht, The Netherlands, pp. 3–180.
[34] Peters, A., Sagar, H., Lantermann, U., and el Moctar, O., 2015, "Numerical Modelling and Prediction of Cavitation Erosion," Wear, **338–339**, pp. 189–201.
[35] Schenke, S., and van Terwisga, T. J. C., 2017, "Numerical Prediction of Vortex Dynamics in Inviscid Sheet Cavitation," 20th Numerical Towing Tank Symposium, Wageningen, The Netherlands, Oct. 1–3, pp. 199–201.
[36] Menter, F., 1994, "Two-Equation Eddy-Viscosity Turbulence Modeling for Engineering Applications," AIAA J., **32**(8), pp. 1598–1605.
[37] Melissaris, T., Bulten, N., and van Terwisga, T. J. C., 2017, "A Numerical Study on the Shedding Frequency of Sheet Cavitation," Seventh International Conference on Computational Methods in Marine Engineering, Nantes, France, May 15–17, pp. 801–812.
[38] Reboud, J.-L., and Delannoy, Y., 1994, "Two-Phase Flow Modelling of Unsteady Cavitation," Second International Symposium on Cavitation, Tokyo, Japan, Apr. 5–7.
[39] Reboud, J.-L., Stutz, B., and Coutier, O., 1998, "Two-Phase Flow Structure of Cavitation: Experiment and Modelling of Unsteady Effects," Third International Symposium on Cavitation, Grenoble, France, Apr. 7–10.
[40] Schnerr, G. H., and Sauer, J., 2001, "Physical and Numerical Modeling of Unsteady Cavitation Dynamics," Fourth International Conference on Multiphase Flow, New Orleans, LA, May 27–June 1.
[41] Schenke, S., and van Terwisga, T. J. C., 2019, "An Energy Conservative Method to Predict the Erosive Aggressiveness of Collapsing Cavitating Structures and Cavitating Flows From Numerical Simulations," J. Multiphase Flow, **111**, pp. 200–218.
[42] Crepier, P., 2017, "Ship Resistance Prediction: Verification and Validation Exercise on Unstructured Grids," Seventh International Conference on Computational Methods in Marine Engineering, Nantes, France, May 15–17, pp. 365–376.
[43] Eca, L., and Hoekstra, M., 2014, "A Procedure for the Estimation of the Numerical Uncertainty of CFD Calculations Based on Grid Refinement Studies," J. Comput. Phys., **262**, pp. 104–130.
[44] Vaz, G., Lloyds, T., and Gnanasundaram, A., 2017, "Improved Modelling of Sheet Cavitation Dynamics on Delft Twist11 Hydrofoil," Seventh International Conference on Computational Methods in Marine Engineering, Nantes, France, May 15–17, pp. 143–156.
[45] Brouwer, J., Tukker, J., and van Rijsbergen, M., 2015, "Uncertainty Analysis of Finite Length Signals," Forth International Conference on Advanced Model Measurement Technologies for the Maritime Industry, Istanbul, Turkey, Sept. 28–30.
[46] Brouwer, J., Tukker, J., and van Rijsbergen, M., 2013, "Uncertainty Analysis and Stationarity Test of Finite Length Time Series Signals," Third International Conference on Advanced Model Measurement Technologies for the Maritime Industry, Gdansk, Poland, Sept. 17–18.
[47] Foeth, E.-J., 2008, "The Structure of Three-Dimensional Sheet Cavitation," Ph.D. thesis, Delft University of Technology, Delft, The Netherlands.
[48] Oprea, A., 2013, "Prediction of Tip Vortex Cavitation for Ship Propellers," Ph.D. thesis, University of Twente, Enschede, The Netherlands.
[49] Muzaferija, S., Papoulias, D., and Peric, M., 2017, "VOF Simulations of Hydrodynamic Cavitation Using the Asymptotic and Classical Rayleigh-Plesset Models," Fifth International Symposium on Marine Propellers, Espoo, Finland, June 12–15, pp. 50–57.
[50] Carrat, J.-B., Fortes-Patella, R., and Franc, J.-P., 2017, "Assessment of Cavitating Flow Aggressiveness on a Hydrofoil: Experimental and Numerical Approaches," ASME Paper No. FEDSM2017-69187.
[51] Li, Z., and van Terwisga, T., 2014, "Assessment of Cavitation Erosion With a URANS Method," ASME J. Fluids Eng., **136**(4), p. 041101.